NMR-based diffusion lattice imaging

Frederik Bernd Laun, Lars Müller, and Tristan Anselm Kuder*
Medical Physics in Radiology, German Cancer Research Center (DKFZ), Im Neuenheimer Feld 280, 69120 Heidelberg, Germany
(Received 24 June 2015; revised manuscript received 13 November 2015; published 7 March 2016)

Nuclear magnetic resonance (NMR) diffusion experiments are widely employed as they yield information about structures hindering the diffusion process, e.g., about cell membranes. While it has been shown in recent articles that these experiments can be used to determine the shape of closed pores averaged over a volume of interest, it is still an open question how much information can be gained in open well-connected systems. In this theoretical work, it is shown that the full structure information of connected periodic systems is accessible. To this end, the so-called "SEquential Rephasing by Pulsed field-gradient Encoding N Time intervals" (SERPENT) sequence is used, which employs several diffusion encoding gradient pulses with different amplitudes. Two two-dimensional solid matrices that are surrounded by an NMR-visible medium are considered: a hexagonal lattice of cylinders and a rectangular lattice of isosceles triangles.

DOI: 10.1103/PhysRevE.93.032401

I. INTRODUCTION

Nuclear magnetic resonance (NMR) diffusion experiments are widely performed to investigate structural barriers hindering the diffusive motion of spin-bearing particles [1,2]. For example, in biomedical imaging, the diffusion coefficient is measured in the context of stroke diagnosis and characterization of tumor tissue [3–7]. More advanced techniques assess additional parameters related to the occurring diffusion restrictions [8–12] or to investigate perfusion effects in the capillary bed [13–17]. Additionally, the course of white matter tracts in biomedical imaging can be reconstructed in great detail, enabling researchers to gain information about the connectivity of different brain regions [18–23]. The structural information can also be used in surgery planning, as surgeons may be able to save important white matter tracts, e.g., the optic radiation [24]. Apart from medical imaging applications, NMR-diffusion experiments are widely performed in porous media research [25–34], because they yield information about the pore shape such as, for example, the typical diameter of pores [35,36]. This information is crucial to characterize the physical properties of many porous media such as concrete or oil-containing rocks.

How much information about the shape of closed pores can be obtained with NMR-based diffusion experiments [37] has been a long-standing question. Indeed, several recent papers have shown the possibility to measure the exact pore shape [38–48]. These findings are, however, only applicable to closed pores, while many porous media have interconnected cavities. It is still an open question if the structure of these connected open porous media can be detected unambiguously with NMR-based diffusion experiments.

In this article, an approach is proposed to extract this information for connected periodic domains. To this end, the "SEquential Rephasing by Pulsed field-gradient Encoding N Time intervals" (SERPENT) sequence is used, which was originally introduced by Stapf *et al.* as a tool to investigate fluid transport [49], and which is a multiple diffusion encoding sequence [50]. It is shown in simulations that it is possible to detect the structure of connected periodic domains based on data acquired with this sequence. In close analogy to x-ray diffraction experiments of periodic crystals, it is a well-known result in the field of NMR diffusion that two short gradient pulses applied to a periodic lattice allow for the determination of the magnitude of diffraction peaks [1]. Here it is demonstrated that—unlike in x-ray scattering—the phase of the diffraction peaks can be directly obtained from additional NMR measurements employing three diffusion weighting gradient pulses. Thus the full spectral information can be obtained, which allows an immediate reconstruction of the shape of the lattice.

II. THEORY

A. Units

The free diffusion coefficient in units of m^2/s is denoted by D_{dim}. The lattice spacing in the x direction in units of meters is denoted by L_{dim}, and the time in units of seconds is denoted by T_{dim}. Dimensionless units are used in the remainder of the manuscript and are defined as follows. The dimensionless time is defined by $T = D_{\mathrm{dim}}\, T_{\mathrm{dim}} L_{\mathrm{dim}}^{-2}$. Quantities of length and inverse length are defined relative to L_{dim}.

B. Definition of the used gradient profiles

The proposed approach is a generalization of double diffusion encoding measurements [50,51] that were shown to yield the shape of arbitrarily shaped closed pores [42]. Recalling that the Larmor frequency is $\omega = -\gamma B$ with the gyromagnetic ratio γ and the magnetic field $B = B_0 + \boldsymbol{G}(t)\boldsymbol{x}(t)$ consisting of the static field B_0 and the gradient field $\boldsymbol{G}(t)$, it follows that the phase acquired by a random walker following the path $\boldsymbol{x}(t)$ is

$$\varphi = -\gamma \int_0^T \boldsymbol{G}(t)\boldsymbol{x}(t)dt, \tag{1}$$

in a reference frame rotating with $\omega_0 = -\gamma B_0$. It is assumed that diffusion weightings are performed by means of the temporal gradient profiles depicted in Fig. 1. In Fig. 1(a), the so-called q-space imaging gradient profile is shown, which can be used to determine the voxel-averaged diffusion propagator [52–55]. Two gradient pulses of duration δ_s and amplitude

*t.kuder@dkfz.de

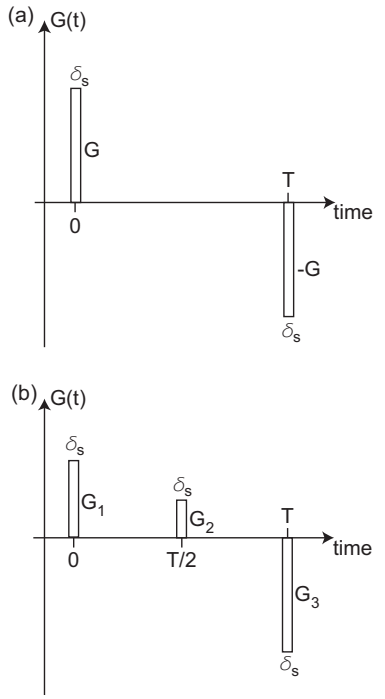

FIG. 1. The gradient profiles used in this manuscript. (a) Classical q-space gradients. (b) The SERPENT sequence with three gradient pulses. Note that the definition of the timing parameter is different from the one in the original SERPENT publication [49].

$\boldsymbol{G}$ are employed generating the wave vector $\boldsymbol{q} = \gamma \boldsymbol{G} \delta_s$. Throughout the manuscript, the narrow pulse approximation, $\delta_s \to 0$, is used, such that this gradient profile is

$$\boldsymbol{G}_{\boldsymbol{q},-\boldsymbol{q}}(t) = \gamma^{-1} \boldsymbol{q} [\delta(t) - \delta(t-T)], \tag{2}$$

with the Dirac delta function $\delta(t)$. The gradient profile in Fig. 1(b) uses three short gradient pulses and is given by

$$\boldsymbol{G}_{\boldsymbol{q}_1,\boldsymbol{q}_2,\boldsymbol{q}_3}(t) = \gamma^{-1} \left[\boldsymbol{q}_1 \delta(t) + \boldsymbol{q}_2 \delta\left(t - \frac{T}{2}\right) + \boldsymbol{q}_3 \delta(t-T) \right]. \tag{3}$$

$\boldsymbol{q}_1$, $\boldsymbol{q}_2$, and $\boldsymbol{q}_3$ do not have to be parallel, but it is required that $\boldsymbol{q}_1 + \boldsymbol{q}_2 + \boldsymbol{q}_3 = 0$ to guarantee that the rephasing condition

$$\int_0^T \boldsymbol{G}(t) dt = \boldsymbol{0} \tag{4}$$

holds true so that particles at rest do not acquire a phase [compare to Eq. (1)]. Furthermore, conventional magnetic resonance phase encoding imaging gradients are considered:

$$\boldsymbol{G}_{\boldsymbol{k}}(t) = \gamma^{-1} \boldsymbol{k} \delta(t). \tag{5}$$

In Eq. (5), the more usual label $\boldsymbol{k}$ was used for $\gamma \boldsymbol{G} \delta_s$. In conventional magnetic resonance imaging, acquiring the NMR signal for a rectangular grid in the so-called $\boldsymbol{k}$ space using the gradients $\boldsymbol{G}_{\boldsymbol{k}}(t)$ can be used to image the measurement object (see, e.g., Chap. 3 of [1]).

C. Signal attenuations

Suppose that a periodic porous material is under investigation and that an NMR-visible medium (e.g., water) diffuses around a solid matrix that is NMR invisible (e.g., rock). A pore space function $\chi(\boldsymbol{x})$ is introduced, which shall be 1 in the diffusing medium and 0 in the solid matrix.

The diffusion weighting induces a signal attenuation,

$$E = \langle \exp(i\varphi) \rangle, \tag{6}$$

where the brackets denote the averaging over all possible random trajectories. Using the gradient profile $G_{\boldsymbol{q},-\boldsymbol{q}}(t)$, the phase that a particle obtains is

$$\varphi = -\boldsymbol{q} \cdot (\boldsymbol{x}_1 - \boldsymbol{x}_2), \tag{7}$$

where $\boldsymbol{x}_1$ and $\boldsymbol{x}_2$ denote the particle positions at the time of the two gradient pulses. The signal attenuation in the long-time limit is (for details see Sec. 7.4 of [1])

$$E_2(\boldsymbol{q}) = \frac{1}{V} \iint d\boldsymbol{x}_1 d\boldsymbol{x}_2 \, \chi(\boldsymbol{x}_1) e^{-i\boldsymbol{q}\cdot\boldsymbol{x}_1} P(\boldsymbol{x}_2, \boldsymbol{x}_1, T) e^{i\boldsymbol{q}\cdot\boldsymbol{x}_2}$$
$$\overset{\text{long } T}{\to} \tilde{\chi}_0(\boldsymbol{q}) [\tilde{f}_{\text{Gauß}}(\boldsymbol{q}, T) * \tilde{\chi}(-\boldsymbol{q})], \tag{8}$$

with the Fourier transform $\tilde{\chi}(\boldsymbol{q})$ of $\chi(\boldsymbol{x})$, the diffusion propagator $P(\boldsymbol{x}_2, \boldsymbol{x}_1, T)$, and the volume V of the NMR-visible medium. In the second line of Eq. (8), where the star denotes a convolution, it is assumed that a Gaussian envelope model [56,57] as described in more detail in Appendix A is appropriate to describe the particle displacement, i.e., that $P(\boldsymbol{x}_2, \boldsymbol{x}_1, T \to \text{large}) \approx \chi(\boldsymbol{x}_1) \chi(\boldsymbol{x}_2) f_{\text{Gauß}}(\boldsymbol{x}_2 - \boldsymbol{x}_1, T)$. The physical reasoning behind this ansatz is twofold. First, particles are never allowed to start or to end up in the solid matrix, which is ensured by the first two terms, $\chi(\boldsymbol{x}_1)$ and $\chi(\boldsymbol{x}_2)$. Second, in the long-time limit, when particles have traveled distances much larger than the lattice spacing, one can interpret the hopping from one unit cell to the adjacent one as being a diffusion step of a large-scale diffusion process with a reduced effective diffusion coefficient. This large-scale diffusion process can be considered to be free as no large-scale boundaries exist, and thus the corresponding propagator is a Gaussian function according to the central limit theorem. This behavior is described by the term $f_{\text{Gauß}}(\boldsymbol{x}_2 - \boldsymbol{x}_1, T)$, which is a properly normalized Gaussian function. The pore space function of the unit cell is labeled $\chi_0(\boldsymbol{x}_1)$, which is identical to $\chi(\boldsymbol{x}_1)$ in the initial unit cell and zero elsewhere. The functions $\tilde{\chi}_0(\boldsymbol{q})$, $\tilde{\chi}(\boldsymbol{q})$, and $\tilde{f}_{\text{Gauß}}(\boldsymbol{q}, T)$ are the Fourier transforms of the functions $\chi_0(\boldsymbol{x})$, $\chi(\boldsymbol{x})$, and $f_{\text{Gauß}}(\boldsymbol{x}, T)$ with respect to $\boldsymbol{x}$. At $T \to \infty$, $f_{\text{Gauß}}(\boldsymbol{x}_2 - \boldsymbol{x}_1, T)$ becomes very broad and $\tilde{f}_{\text{Gauß}}(\boldsymbol{q}, T)$ narrows down, so that $E_2(\boldsymbol{q})$ is essentially equal to $|\tilde{\chi}(\boldsymbol{q})|^2$.

Owing to the periodicity of $\chi(\boldsymbol{x})$, $\tilde{\chi}(\boldsymbol{q})$ is related to the structure factor $S(\boldsymbol{q})$ known from crystallography,

$$\tilde{\chi}(\boldsymbol{q}) = V_Z^{-1} S(\boldsymbol{q}) = V_Z^{-1} \cdot \begin{cases} \sum_l f_l(\boldsymbol{G}_R) \exp(-i \boldsymbol{G}_R \cdot \boldsymbol{r}_l) & \text{if } \boldsymbol{q} = \boldsymbol{G}_R \\ \sim 0 \quad \text{otherwise} \end{cases}, \tag{9}$$

where $\boldsymbol{G}_{\mathrm{R}}$ is a vector of the reciprocal lattice and V_{Z} the volume of the NMR-visible medium in one unit cell. In close analogy to crystallography, $f_l(\boldsymbol{q}) = \int_{\mathrm{cell}} \rho_l(\boldsymbol{r}') \exp(-i\boldsymbol{q}\cdot\boldsymbol{r}')d\boldsymbol{r}'$ are the form factors of the "atoms" with density $\rho_l(\boldsymbol{r})$ residing at positions $\boldsymbol{r}_l$ within the Wigner-Seitz cell. In connected open systems, it usually makes sense to consider the basis to be "single atomic", a case for which Eq. (9) may be restated as

$$\tilde{\chi}(\boldsymbol{q}) = \begin{cases} \tilde{\chi}_0(\boldsymbol{q}) & \text{if } \boldsymbol{q} = \boldsymbol{G}_{\mathrm{R}} \\ \sim 0 & \text{otherwise} \end{cases}, \tag{10}$$

where $\tilde{\chi}_0(\boldsymbol{q}) = V_{\mathrm{Z}}^{-1} \int_{\mathrm{cell}} \chi(\boldsymbol{r}) \exp(-i\boldsymbol{q}\cdot\boldsymbol{r}')d\boldsymbol{r}'$. Thus, for an infinite, perfect lattice, signal peaks arise at certain points of the reciprocal lattice and the signal attenuation $E_2(\boldsymbol{q})$ consists of Bragg's peaks as in crystallography, where $\boldsymbol{q}$ would correspond to the difference of wave vectors of incoming and outgoing wave ($\boldsymbol{k}_{\mathrm{out}} - \boldsymbol{k}_{\mathrm{in}}$). As mentioned, the peaks are broadened by a Gaussian envelope at finite diffusion times, which originates from the Gaussian envelope of the diffusion propagator (see Appendix A and Eq. (7.33) of [1]), but not from the lattice size as in crystallography.

A crucial difference between q-space imaging and crystallography is the reason for the disappearance of the phase information. In crystallography, the detector is insensitive to the phase. But in q-space imaging, the signal is phaseless and thus the phase-sensitive detector cannot resolve it.

This difference opens the door for alterations of the experiment that preserve the phase information, e.g., by using $\boldsymbol{G}_{\boldsymbol{q}_1,\boldsymbol{q}_2,\boldsymbol{q}_3}(t)$ instead of $\boldsymbol{G}_{\boldsymbol{q},-\boldsymbol{q}}(t)$. In this case, the signal attenuation can be expressed by (see also [50])

$$E_3(\boldsymbol{q}_1,\boldsymbol{q}_2,\boldsymbol{q}_3) = \tilde{\chi}(\boldsymbol{q}_1)\tilde{\chi}(\boldsymbol{q}_2)\tilde{\chi}(\boldsymbol{q}_3) = V_{\mathrm{Z}}^{-3} S(\boldsymbol{q}_1)S(\boldsymbol{q}_2)S(\boldsymbol{q}_3). \tag{11}$$

Again, at finite diffusion times, the peaks are broadened by a Gaussian envelope, whose width decreases with increasing diffusion time (see Appendix A). Nonzero values of $E_3(\boldsymbol{q}_1,\boldsymbol{q}_2,\boldsymbol{q}_3)$ can only arise if the three vectors $\boldsymbol{q}_1$, $\boldsymbol{q}_2$, and $\boldsymbol{q}_3$ are vectors of the reciprocal lattice.

D. Determination of the pore space function

The experimental aim is to measure $\tilde{\chi}(\boldsymbol{q})$ and to determine $\chi(\boldsymbol{x})$ therewith. The magnitude of $\tilde{\chi}(\boldsymbol{q})$ and the position of the peaks can be obtained by measurements with $\boldsymbol{G}_{\boldsymbol{q},-\boldsymbol{q}}(t)$ and setting $|\tilde{\chi}(\boldsymbol{q})| = |E_2(\boldsymbol{q})|^{1/2}$. The problem of how to determine the phase of $\tilde{\chi}(\boldsymbol{q})$ in diffusion MR has, however, been unresolved so far.

1. Connection between the phases of the peaks

According to Eq. (11), the relationship between the phases $\psi(\boldsymbol{q}_1,\boldsymbol{q}_2,\boldsymbol{q}_3) = \arg[E_3(\boldsymbol{q}_1,\boldsymbol{q}_2,\boldsymbol{q}_3)]$ and $\phi(\boldsymbol{q}) = \arg[\tilde{\chi}(\boldsymbol{q})]$ is

$$\psi(\boldsymbol{q}_1,\boldsymbol{q}_2,\boldsymbol{q}_3) = \phi(\boldsymbol{q}_1) + \phi(\boldsymbol{q}_2) + \phi(\boldsymbol{q}_3). \tag{12}$$

The phase $\psi(\boldsymbol{q}_1,\boldsymbol{q}_2,\boldsymbol{q}_3)$ is obtainable from measurements, but the phases $\phi(\boldsymbol{q}_i)$ of $\tilde{\chi}(\boldsymbol{q}_i)$ are only accessible as sums corresponding to three reciprocal lattice points at which the structure factor is not equal to zero. In matrix notation, this relation can be stated as

$$\boldsymbol{\psi} = A\boldsymbol{\phi}, \tag{13}$$

with the following definitions. The nth triple of probed q-vectors, which shall be labeled with the natural number indices u_n, v_n, and w_n, is $\boldsymbol{q}_{u_n}$, $\boldsymbol{q}_{v_n}$, and $\boldsymbol{q}_{w_n}$. Using the short-hand notation $\phi(\boldsymbol{q}_m) = \phi_m$ and $\psi(\boldsymbol{q}_{u_n},\boldsymbol{q}_{v_n},\boldsymbol{q}_{w_n}) = \psi_n$, the elements of $\boldsymbol{\phi}$ are ϕ_m, the elements of $\boldsymbol{\psi}$ are ψ_n, and the elements of the matrix A are $A_{n,m} = \delta_{m,u_n} + \delta_{m,v_n} + \delta_{m,w_n}$. It should be noted that A must fulfill the demand that the system of equations defined by Eq. (13) must be uniquely solvable (except for lattice shifts; see Sec. II D2), which is, figuratively, equivalent to the demand that no disconnected set of q-vectors $\boldsymbol{q}_{u_n}$, $\boldsymbol{q}_{v_n}$, and $\boldsymbol{q}_{w_n}$ exist. Otherwise the proposed approach cannot be used.

The task is to invert this system of equations and to determine $\boldsymbol{\phi}$.

2. Fixing of phases of initial peaks

Equation (13) does not uniquely define the reconstructed lattice image, since the experimental information is obtained by means of a diffusion experiment, which detects displacements, but is blind to absolute positions. Consequently, the actual position of the lattice cannot be determined and one must restrain oneself to reconstruct an image of undefined absolute position. This freedom in shifting the reconstructed image along one direction is equivalent to the freedom of adding an arbitrary linear phase in q-space. Thus, when solving Eq. (13), an additional modulation by an arbitrary linear phase may be chosen along each axis of q space, i.e., for example, along $\boldsymbol{q}_1$, $\boldsymbol{q}_2$ in two dimensions; and along $\boldsymbol{q}_1$, $\boldsymbol{q}_2$, $\boldsymbol{q}_3$ in three dimensions with linearly independent q-vectors. Therefore, in two dimensions, the phases of $\tilde{\chi}(\boldsymbol{q})$ at the central peak at $\boldsymbol{q}_1 = \boldsymbol{0}$ and at two further peaks at $\boldsymbol{q}_2$ and $\boldsymbol{q}_3$, with $\boldsymbol{q}_2$ not parallel to $\boldsymbol{q}_3$, can be chosen arbitrarily, since setting these phases merely corresponds to shifting the reconstructed image. Accordingly, in three dimensions, the phases of $\tilde{\chi}(\boldsymbol{q})$ at the central peak at $\boldsymbol{q}_1 = \boldsymbol{0}$ and of three further peaks at $\boldsymbol{q}_2$, $\boldsymbol{q}_3$, and $\boldsymbol{q}_4$ can be chosen arbitrarily. A straightforward approach is to set these phases to zero, i.e., $\phi_1 = \phi_2 = \phi_3 = 0$ in two dimensions. In this article, it is assumed that $\chi(\boldsymbol{x})$ is real and hence $\tilde{\chi}(-\boldsymbol{q}) = \tilde{\chi}^*(\boldsymbol{q})$. Accordingly, the phases ϕ at $-\boldsymbol{q}_2$ and $-\boldsymbol{q}_3$ are equal to zero as well.

3. Determination of the peak phases

A complication in inverting Eq. (13) arises from the fact that phases are only detectable for modulus 2π, such that a straightforward inversion, e.g., by means of the pseudoinverse of A, is in general not successful. An alternative straightforward approach to solve Eq. (13) is to minimize

$$\arg(\exp(i(\boldsymbol{\psi} - A\boldsymbol{\phi})))^2. \tag{14}$$

4. k-Space lattice imaging

Using the gradient profile $\boldsymbol{G}_{\boldsymbol{k}}(t)$, the phase that a particle resting at position $\boldsymbol{x}$ obtains is $\varphi = -\boldsymbol{k}\cdot\boldsymbol{x}$. Diffusion is irrelevant here, since it is assumed that only one gradient pulse of infinitesimal duration is applied when using $\boldsymbol{G}_{\boldsymbol{k}}(t)$. The corresponding signal attenuation is $E_1(\boldsymbol{k}) = \exp(-i\boldsymbol{k}\cdot\boldsymbol{x}) = \tilde{\chi}(\boldsymbol{k})$. $E_1(\boldsymbol{k})$ is only unequal to zero at the reciprocal lattice points, for which $\tilde{\chi}(\boldsymbol{k})$ is unequal to zero. Thus, for a perfect lattice, $\tilde{\chi}(\boldsymbol{k})$ can be directly obtained by applying k-vectors that

hit the Bragg peaks. This approach can be considered to be a special version of conventional magnetic resonance imaging, where the spacing between the sampled k-vectors is adapted to the sample. This adaption makes the therefrom resulting field of view equal to the spacing of the lattice cells. An alternative interpretation of this experiment in position space is that the field of view is adapted such that the wrapping artifacts of conventional magnetic resonance imaging phase encoding are adjusted such that the images of all neighboring unit cells add up coherently.

If lattice defects are present, the global nature of this approach obscures the information about $\tilde{\chi}(\boldsymbol{k})$. Say that dislocations are present introducing N shifts $\boldsymbol{x}_{\text{shift},n}$ with $n \in \{1, \ldots, N\}$ of different subparts of the lattice. Then the signal attenuation becomes $E_1(\boldsymbol{k}) = \sum_{n=1}^{N} \tilde{\chi}_n(\boldsymbol{k}) \exp(-i\boldsymbol{k} \cdot \boldsymbol{x}_{\text{shift},n})$ with $\tilde{\chi}_n(\boldsymbol{k})$ corresponding to the Fourier transform of the nth lattice subpart $\chi_n(\boldsymbol{x})$. The exponential factors $\exp(-i\boldsymbol{k} \cdot \boldsymbol{x}_{\text{shift},n})$ eventually can lead to a complete vanishing of $E_1(\boldsymbol{k})$ at $\boldsymbol{k} \neq 0$ and then this direct imaging approach becomes unfeasible.

Diffusion lattice imaging tends to behave differently in this situation, because particles will usually only explore the nearby unit cells, but not the complete lattice. In this case, the particles will at most traverse a few dislocations. Relative to the unit cell, where the considered particle starts, the dislocation $\boldsymbol{x}_{\text{shift},n}$ can therefore be assumed to be small. Otherwise the initial assumption that one deals with continuous lattices would not be valid. In this case, $\exp(-i\boldsymbol{k} \cdot \boldsymbol{x}_{\text{shift},n}) \approx 1$ and hence the approach as described in Secs. II D1–II D3 can still be applied with expectedly reasonable accuracy.

III. METHODS

A. Monte Carlo simulations

Monte Carlo simulations were performed using in-house developed Monte Carlo code, which was implemented in MATLAB (MathWorks, Natick, MA).

A random walk in two two-dimensional periodic lattices was simulated. The lattices were a hexagonal lattice of cylinders [Fig. 2(a)] and a rectangular lattice of triangles [Fig. 2(b)], which resembles a saw tooth function in the x and y directions. The NMR-visible medium was assumed to be diffusing between the cylinders or triangles, which form the solid matrix inaccessible to the diffusing particles. The separation of adjacent unit cells was $L_x + dL_x$ in the x direction and $L_y + dL_y$ in the y direction. For the rectangular lattice, $L_x = 1$ and $L_y = 1$. For the hexagonal lattice $L_x = 1$ and $L_y = \sqrt{3}$. dL_x and dL_y are random variables distributed according to a Gaussian function with widths σ_{L_x} and σ_{L_y}. Two cases were considered: firstly, a perfect lattice with $\sigma_{L_x} = \sigma_{L_y} = 0$ and, secondly, an imperfect lattice with $\sigma_{L_x} = 0.1$ and $\sigma_{L_y} = 0.1$. An array of $10^5 \times 10^5$ cylinders or triangles was generated once and then used for all random walkers. The initial particle position was generated randomly, but had to stay 50 cylinders or triangles apart from the boundary to avoid particles leaving the defined lattice during the random walk. The radius of the cylinders was 0.48. The length of the short triangle edges is 0.96. Thus, there is a separation between the restricting barriers so that the spins can diffuse in the whole lattice.

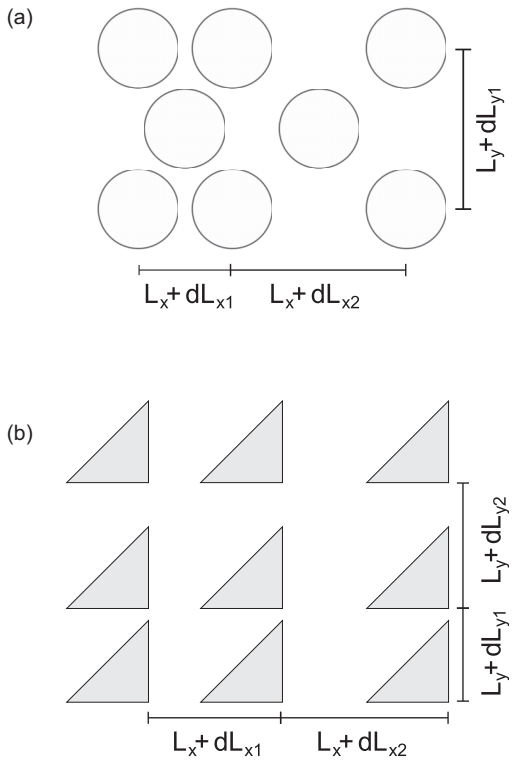

FIG. 2. The lattices used in the Monte Carlo simulations. (a) A hexagonal lattice of solid cylinders. The particles may only reside in the white region, and not within the cylinders. (b) A rectangular lattice of isosceles triangles. As for the cylinders, the random walkers can only access the area between the triangles. For the nonperfect lattice, dL_{xi} and dL_{yi} are obtained from the Mersenne random number generator to vary the locations of the diffusion restrictions.

Each random step is simulated as follows. A random displacement distributed equally in the interval $[-\sqrt{3}dr; \sqrt{3}dr]$, which results in an average square root displacement for one step of dr, is generated with a Mersenne random number generator [58] in the x and in y directions, respectively. The random step is only accepted if the particle does not end up in the solid matrix. Otherwise new random steps are generated until the particle ends up in the space that is not covered by the solid matrix.

The following parameters were used: 5×10^6 random walkers, $T = 3$, number of time steps $N_{\text{step}} = 2.4 \times 10^5$ per time unit, step duration $\tau \approx 4.2 \times 10^{-6}$, and step length $dr = \sqrt{2\tau} \approx 2.9 \times 10^{-3}$.

The particle positions at times 0, $T/2$, and T were stored in a data file. The particle positions were used to calculate the signal attenuations $E_1(\boldsymbol{q})$, $E_2(\boldsymbol{q})$, and $E_3(\boldsymbol{q}_1, \boldsymbol{q}_2, \boldsymbol{q}_3)$ at $T = 3$ in MATLAB. Code that reproduces the figures is provided as Supplemental Material [59].

B. Reconstruction of the lattice images

Figure 3 shows the reciprocal lattice points that were used for the reconstruction for the cylinder lattice [Fig. 3(a), 31 points] and for the triangle lattice [Fig. 3(b), 13 points]. Here, it is assumed that the position of the peaks is known *a priori*.

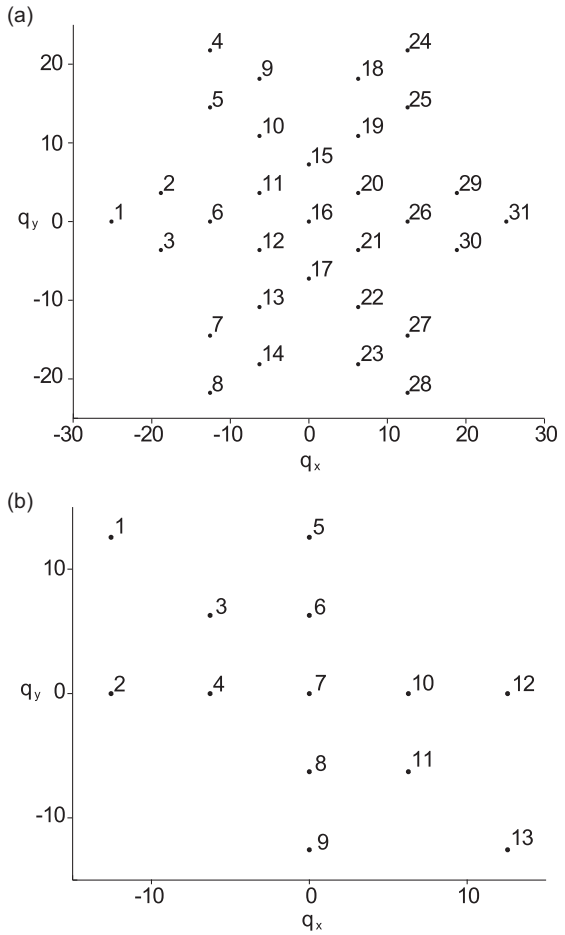

FIG. 3. Points of the reciprocal lattice that were used in the reconstruction for (a) the cylinder lattice and (b) the triangle lattice. In (a), the spacing between points is $2\pi \approx 6.28$ along the x direction and $4\pi/\sqrt{3} \approx 7.26$ along the y direction. In (b), the spacing is 2π along both directions.

In experiments, one would determine the position of the peaks by measurements of $E_2(\boldsymbol{q})$.

For the cylinder lattice, the phases ϕ at the peaks 16, 20, and 21 were set to zero, which inflicts that the phases ϕ at the peaks 11 and 12 are also zero due to the condition $\tilde{\chi}(\boldsymbol{q}) = \tilde{\chi}^*(-\boldsymbol{q})$. For the triangle lattice, the phases ϕ at the peaks 7, 8, and 10 were set to zero, which inflicts that also the phases ϕ at the peaks 4 and 6 equal zero. The indices u_n, v_n, and w_n of the q-vector triples $\boldsymbol{q}_{u_n}$, $\boldsymbol{q}_{v_n}$, and $\boldsymbol{q}_{w_n}$ used for the reconstruction are stated in Table I for the cylinder lattice and in Table II for the triangle lattice. These q-vector triples represent one particular example and other combinations are possible. $\boldsymbol{\phi}$ was determined using the simulation data by minimizing $\arg(\exp(i(\boldsymbol{\psi} - A\boldsymbol{\phi})))^2 + \boldsymbol{\phi}_0^2$ with the Quasi-Newton method in MATLAB and $\boldsymbol{\phi} = 1$ and $\boldsymbol{\phi}_0 = 0$ were set as initial values for both lattices. $\boldsymbol{\phi}_0$ is a vector containing the phases of the peaks that shall have zero phase, i.e., $\boldsymbol{\phi}_0 = (\phi_{11},\phi_{12},\phi_{16},\phi_{20},\phi_{21})^T$ and $\boldsymbol{\phi}_0 = (\phi_4,\phi_6,\phi_7,\phi_8,\phi_{10})^T$ for the cylinder lattice and triangle lattice, respectively.

Images $I(\boldsymbol{x})$ of the lattices were reconstructed with an image matrix of 300×300 and image dimensions of 3×3 by computing $I(\boldsymbol{x}) = \sum_n |E_2(\boldsymbol{q}_n)|^{1/2} \exp(i\phi_n) \exp(i\boldsymbol{x} \cdot \boldsymbol{q}_n)$ with n ranging from 1 to 31 for the cylinder lattice, and n ranging from 1 to 13 for the triangle lattice. For comparison, a k-space-based image was computed by $I_{\mathrm{k-space}}(\boldsymbol{x}) = \sum_n E_1(\boldsymbol{q}_n) \exp(i\boldsymbol{x} \cdot \boldsymbol{q}_n)$.

TABLE I. Indices of sampled q-vector triples for the cylinder lattice.

$n = u_n$	v_n	w_n
1	26	26
2	21	26
3	20	26
4	22	22
5	22	21
6	20	21
7	19	20
8	19	19
9	17	22
10	17	21
11	17	20
12	15	21
13	20	15
14	19	15
15	12	21
17	11	20
18	13	17
19	12	17
20	11	17
21	15	12
22	11	15
23	10	15
24	13	13
25	12	13
26	11	12
27	10	11
28	10	10
29	12	6
30	6	11
31	6	6

IV. RESULTS OF SIMULATIONS

A. Scatter plots

Figure 4 visualizes the particle distributions at time $T = 0$ [Figs. 4(a) and 4(b)] and $T = 3$ [Figs. 4(c) and 4(d)] that

TABLE II. Indices of sampled q-vector triples for the triangle lattice.

n	u_n	v_n	w_n
1	12	4	4
2	2	10	10
3	5	8	8
4	9	6	6
5	13	3	3
6	1	11	11
7	11	4	6
8	3	10	8

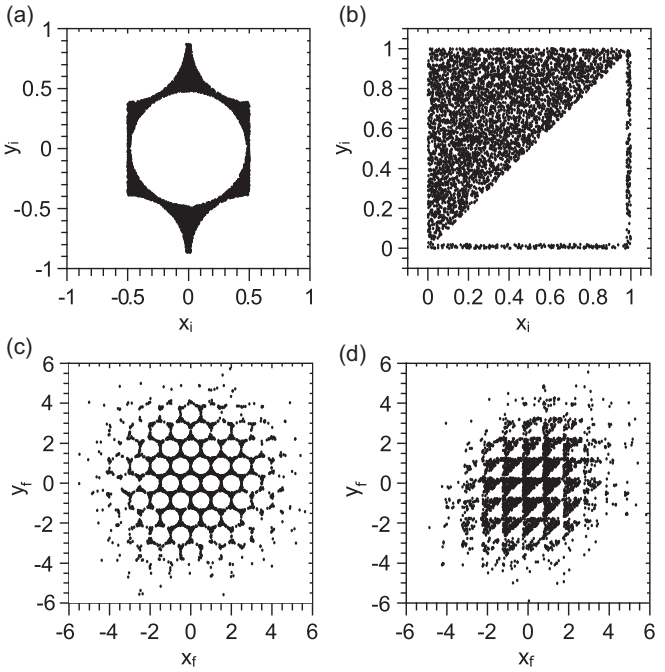

FIG. 4. Particle distributions. Left column: hexagonal lattice of solid cylinders. Right column: rectangular lattice of isosceles triangles. (a,b) Starting positions in initial unit cell. (c,d) Particle positions at $T = 3$. Five thousand of the 5×10^6 particles are shown; σ_{L_x} and σ_{L_y} are zero.

were obtained by the Monte Carlo simulations. The particle positions $(x_\mathrm{i},\ y_\mathrm{i})$ in their initial unit cell are shown in Figs. 4(a) and 4(b). Owing to the diffusion process, they distribute over the lattice; in Figs. 4(c) and 4(d), the final particle positions $(x_\mathrm{f},\ y_\mathrm{f})$ with respect to their initial unit cell are plotted.

B. q-Space spectra

Figure 5 shows $|E_2(\boldsymbol{q})|^{1/2}$ for the hexagonal cylinder array [Fig. 5(a)] and the rectangular array of triangles [Fig. 5(b)] obtained using the Monte Carlo simulations. Due to the periodicity of $\chi(\boldsymbol{x})$, $\tilde{\chi}(\boldsymbol{q})$ is zero except for certain q values, where Dirac delta function peaks arise, which are visible in Fig. 5, and which are broadened due to the finite diffusion time (see Appendix A).

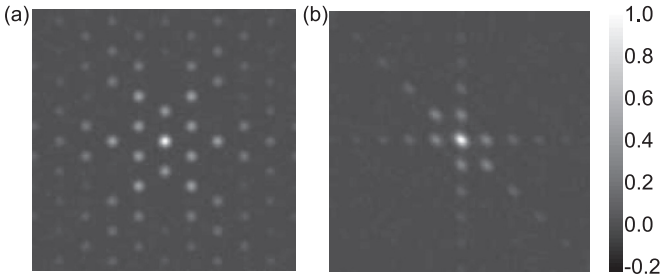

FIG. 5. $|E_2(\boldsymbol{q})|^{1/2}$ for the hexagonal cylinder lattice (a) and the rectangular lattice of triangles (b) for $|q_x| \leqslant 10\pi$ and $|q_y| \leqslant 10\pi$, where the x direction is left-right in the image and σ_{Lx} and σ_{Ly} are zero. Owing to the periodicity of the lattice, signal peaks arise at certain q values, which is analogous to diffraction experiments.

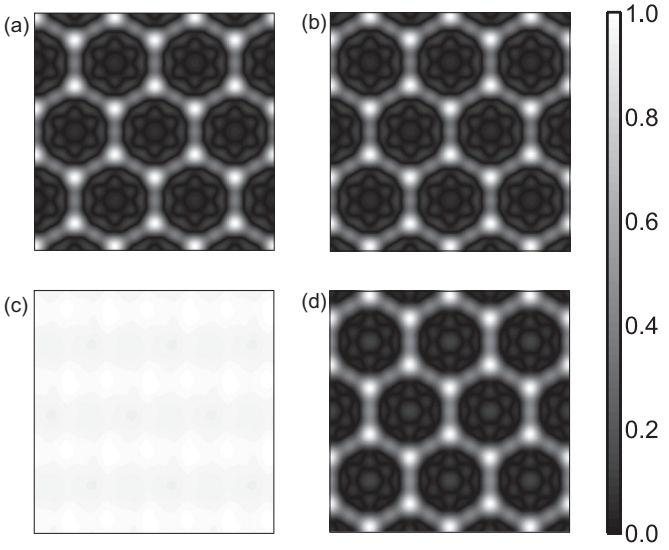

FIG. 6. Reconstructed lattice images. (a,b) Perfect lattice with $\sigma_{Lx} = 0$ and $\sigma_{Ly} = 0$. (c,d) Imperfect lattice with $\sigma_{Lx} = 0.1$ and $\sigma_{Ly} = 0.1$. (a,c) The images are reconstructed with conventional magnetic resonance imaging. (b,d) The images are reconstructed with the diffusion lattice imaging approach. The structural information in (c) is lost, because the signal at the peaks vanishes at $\boldsymbol{k} \neq \boldsymbol{0}$ as described in Sec. II D4 and only the signal peak at $\boldsymbol{k} = \boldsymbol{0}$ survives. The image in (c) is thus essentially the Fourier transform of $\delta(\boldsymbol{x})$, which equals unity. This results in a white area with very faint structures, which are not related to the matrix structure.

Figure 6 shows the magnitude of the reconstructed images for the hexagonal cylinder array.

In the top row [Figs. 6(a) and 6(b)], the lattice was "perfect" with σ_{Lx} and σ_{Ly} set to zero. Then, the k-space-based images reconstructed from $E_1(\boldsymbol{k})$ [Fig. 6(a)] and those reconstructed using diffusion lattice imaging [Fig. 6(b)] yield identical results. In both cases, the structure of the lattice is clearly appreciable, although smearing effects are visible owing to the low number of used signal peaks. In the bottom row [Figs. 6(c) and 6(d)], the lattice is nonperfect with $\sigma_{Lx} = 0.1$ and $\sigma_{Ly} = 0.1$. In this case, the k-space-based image reconstruction cannot resolve the lattice [Fig. 6(c)], while diffusion lattice imaging still yields an image of decent quality with a slightly increased smearing [Fig. 6(d)]. In Fig. 6(c), the reconstructed image has an almost constant intensity. Here, all peaks except for the central peak vanish due to dephasing caused by the nonperfect lattice (see Sec. II D4). Hence the image is essentially the Fourier transform of $\delta(\boldsymbol{x})$, which equals unity. In real experiments, the lattice is presumably not perfect and thus only diffusion lattice imaging can resolve it. Figure 7 shows the corresponding images for the rectangular lattice of triangles, where the same effects as in Fig. 6 are visible.

V. DISCUSSION

In this work, an approach was introduced that enables the unambiguous reconstruction of periodic lattices with NMR-based diffusion experiments. It has been well known since the early 1990s [1,52–54,60] that the magnitude spectrum $E_2(\boldsymbol{q})$,

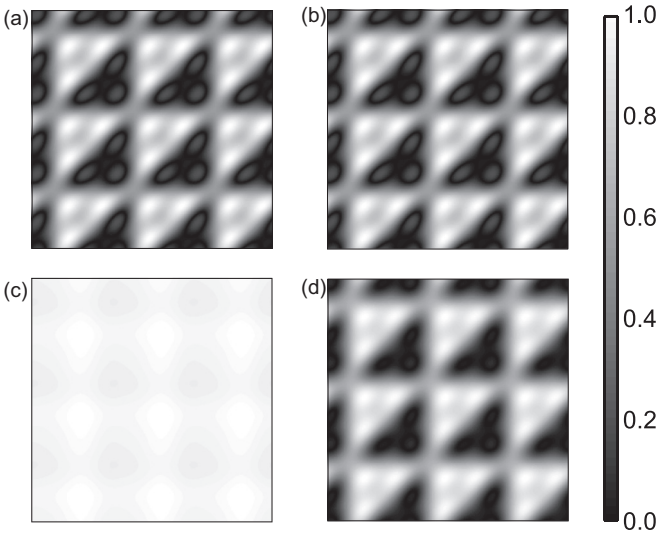

FIG. 7. Reconstructed lattice images. (a,b) Perfect lattice with $\sigma_{Lx} = 0$ and $\sigma_{Ly} = 0$. (c,d) Imperfect lattice with $\sigma_{Lx} = 0.1$ and $\sigma_{Ly} = 0.1$. (a,c) The images are reconstructed with conventional magnetic resonance imaging. (b,d) The images are reconstructed with the diffusion lattice imaging approach. As in Fig. 6, the matrix structure cannot be recovered in (c) due to the variations of the lattice spacing resulting in a mainly white image.

and thus $|\tilde{\chi}(\boldsymbol{q})|$, could be obtained for these structures, but how to obtain the phase information was elusive.

This problem is closely related to the question of whether NMR-based diffusion experiments might be suited to uniquely reconstruct *closed* pores hindering the diffusion process. As for open periodic lattices, it had been known for a long time that $|\chi(\boldsymbol{q})|$ could be obtained [1,52–54,60] but, again, it had not been clear how to extract the phase information. For closed pores, this problem was solved in a recent series of articles, where two distinct approaches were presented that are based on two different classes of temporal gradient profiles. Firstly, the class of long-narrow gradient profiles can be used [38,39,44,45]. Using these profiles, the obtained signal becomes the Fourier transform of the pore space function of the average pore in the sample, thus allowing one to reconstruct pore shape distributions. Secondly, an iterative approach was introduced using the class of narrow-only gradient profiles, which consist only of short gradient pulses [40–43,49–51,61]. This narrow-only class provides better convergence properties to the long-time limit, but if the sample contains a distribution of pore shapes, it cannot be applied straightforwardly [41,43,48].

The work at hand generalizes the latter approach of narrow-only gradient profiles, so that it becomes applicable to open periodic lattices. The application to lattices comes with certain complications, which are not present for closed pores. In particular, $\tilde{\chi}(\boldsymbol{q})$ and the resulting NMR signal of closed pores are continuous, while both have discrete peaks at certain q vectors for connected periodic lattices. This entails that the q vectors have to be adjusted properly for periodic lattices to hit the peaks, especially for the three-gradient measurement to obtain the phases. The experimental application of the correct q vectors and the reconstruction thus may become rather cumbersome, but we are not aware of a more direct or general approach. For example, the long-narrow gradient profile, which is so successful in unveiling closed pore shapes, does not yield the necessary information to reconstruct connected lattices (see Appendix B).

The phase problem is ubiquitously present in physics, and in particular in x-ray crystallography, where several approaches have been developed to solve it (see, e.g., the reviews [62–64]). On the one hand, techniques like molecular replacement, isomorphous replacement, anomalous dispersion, and multiple wavelength anomalous diffraction make use of physical properties of the sample, e.g., by using K edges or by investigating physically altered crystals. On the other hand, direct methods like the "Shake-and-Bake" algorithm aim at resolving the crystal structure directly. For structures containing as many as 1000 nonproton atoms, these direct methods work well such that the phase problem can mainly be regarded as solved in this regime. Another interesting approach is the multibeam diffraction technique [65], where peaks of different beams are superimposed yielding information about their relative phase information similarly to Eq. (12). As in NMR-based diffusion lattice imaging, the coincidence of peaks must be properly adjusted following this approach.

Concerning the practical impact of NMR-based diffusion lattice imaging, one must admit that, unlike in crystallography, there are few real systems that are connected, periodic, and of major interest to researchers relying on NMR-diffusion experiments. One important aspect is that one is restricted to length scales in the micrometer range for water diffusion, because the gradient coils available nowadays do not permit the application of stronger gradients and thus of higher q values, which would correspond to shorter length scales. Thus diffusion lattice imaging of molecular crystals is not feasible. Nonetheless, there are numerous publications dealing with NMR-based diffusion experiments in periodic domains (e.g. [60,66–71]), because these systems are rather easy to handle mathematically while they can still provide physical insights. Thus, we consider the findings presented here to be foremost of theoretical interest, which, however—as it is often in physics—may pave the way to applications to more complex systems.

The open question at this point is how much information can be obtained in nonperiodic open domains. Any advance in this regard would be highly valuable. One might ask a general question: If the domain is random, is it still useful to think about acquiring NMR-based diffusion images of any kind? Definitely, one can construct domains that are "too random," but there is a large class of domains that might have reasonable properties in this regard. Regarding impermeable domains, consider, for example, the following setup. A domain is open, but many solid grains are present, which may be of equal or of varying shape, and which reside at random positions. Diffusion tensor fiber phantoms as described, e.g., in [71–74] are an example for such domains. It would be interesting to acquire an image of these grains. However, if the lattice periodicity is lost, the signal peaks tend to vanish, and it is unclear at this stage how an image of the grains can be retrieved. Moreover, it has been recently pointed out that diffusion pore imaging techniques that rely on short gradient pulses do not yield the arithmetically averaged pore image, because the average

of the product is not equal to the product of the averages [41,43,48]. The same holds true for diffusion lattice imaging. Even if the grains are aligned perfectly periodically, one cannot straightforwardly measure an average grain if the grains are shaped differently. One presumably must restrict oneself to measuring "average structure factors" (see p. 336 of [55]).

For permeable boundaries, the task is even harder. Consider, for example, the typical setup found in tissue. The cell membrane is very thin, and it seems unfeasible to treat the membrane as a solid matrix and make an image of this matrix. Thus peaks, as they appear in Fig. 5, cannot be present, as they basically describe the void spaces of the pore space function. Thus one must rely on the restricting properties of the membrane. As the diffusion pore imaging and lattice imaging approaches presented so far all require that the diffusion process is in the long-time limit, intra- and extracellular compartments are mixed up and are not separable any more. It is challenging to retrieve the information about the cell shape in this scenario.

In principle, periodic lattices can be imaged with conventional MR imaging as described in Sec. II D4. Slight imperfections of the lattice prevent this approach, however, from being successful. Diffusion lattice imaging solves this problem for a wide range of crystal imperfections such as random translations. One must, however, be aware of the fact that lattice imperfections that produce global rotations are not intrinsically compensated by diffusion lattice imaging and thus the reconstruction becomes difficult for such lattice imperfections.

In conclusion, an approach has been proposed to reconstruct the shape of periodic lattices with NMR-based diffusion experiments. This is a report on an unambiguous structure determination with this technique for domains that are not completely closed.

ACKNOWLEDGMENT

Financial support by the Deutsche Forschungsgemeinschaft is gratefully acknowledged (Grants No. LA 2804/1-3, No. LA 2804/2-1, and No. KU 3362/1-1).

APPENDIX A: GAUSSIAN ENVELOPE MODEL AND LINEWIDTH

One reasonable approach to describe the particle distribution at large but finite diffusion times is to use a Gaussian envelope model [56,57]:

$$P(\boldsymbol{x}_2,\boldsymbol{x}_1,T\rightarrow\text{large})\approx\chi(\boldsymbol{x}_1)\chi(\boldsymbol{x}_2)f_{\text{Gauß}}(\boldsymbol{x}_2-\boldsymbol{x}_1,T). \tag{A1}$$

In two dimensions, the elements of the covariance matrix Σ associated to $f_{\text{Gauß}}(\boldsymbol{x}_2-\boldsymbol{x}_1,T)$ are labeled as

$$\Sigma=\begin{pmatrix}\sigma_{xx}^2 & \sigma_{xy}^2\\ \sigma_{xy}^2 & \sigma_{yy}^2\end{pmatrix}. \tag{A2}$$

The simulated covariance matrices at $T=3$ were

$$\Sigma_{\text{O}}=\begin{pmatrix}2.714 & 0.005\\ 0.005 & 2.685\end{pmatrix} \tag{A3}$$

for the hexagonal array of cylinders, and

$$\Sigma_{\Delta}=\begin{pmatrix}2.264 & 0.646\\ 0.646 & 2.264\end{pmatrix} \tag{A4}$$

for the rectangular lattice of triangles (see also Appendix C).

Using the Gaussian envelope approach, Eq. (11) becomes

$$\begin{aligned}E_3(\boldsymbol{q}_1,\boldsymbol{q}_2,\boldsymbol{q}_3)\approx\int\int\int d\boldsymbol{x}_1 d\boldsymbol{x}_2 d\boldsymbol{x}_3\frac{\chi(\boldsymbol{x}_1)}{V}e^{-i\boldsymbol{q}_1\cdot\boldsymbol{x}_1}\\ \times\chi(\boldsymbol{x}_2)f_{\text{Gauß}}(\boldsymbol{x}_2-\boldsymbol{x}_1,T/2)e^{-i\boldsymbol{q}_2\cdot\boldsymbol{x}_2}\\ \times\chi(\boldsymbol{x}_3)f_{\text{Gauß}}(\boldsymbol{x}_3-\boldsymbol{x}_2,T/2)\,e^{-i\boldsymbol{q}_3\cdot\boldsymbol{x}_3},\end{aligned} \tag{A5}$$

with the integrals ranging over the whole lattice. It is assumed that one can distinguish three distinct length scales. One scale is defined by the lattice spacing. A larger scale is defined by the size of the Gaussian envelope, which should span many lattice cells and is responsible for the broadening of the peaks of E_2 and E_3. An even larger scale corresponds to the overall sample size. In real systems, this scale is assumed to be unreachable for diffusing molecules. Thus, although the sample or crystallite size defines the width of the Bragg's peak in x-ray diffraction experiments, it is assumed to be irrelevant here. The peak width is determined by the size of the Gaussian envelope of the diffusion propagator as shown below. It should be noted that the process is assumed to be time invariant; i.e., $f_{\text{Gauß}}(\boldsymbol{x}_2-\boldsymbol{x}_1,T/2)$ is the same function as $f_{\text{Gauß}}(\boldsymbol{x}_3-\boldsymbol{x}_2,T/2)$.

Assume that all particles start in the same initial unit cell of a periodic open domain. This unit cell shall contain the origin $\boldsymbol{x}=\boldsymbol{0}$ of the coordinate system. The pore space function of the unit cell shall be labeled $\chi_0(\boldsymbol{x}_1)$, which is identical to $\chi(\boldsymbol{x}_1)$ in the initial unit cell and zero elsewhere. The resulting signal attenuation is the same as for arbitrary starting points distributed in the whole lattice, since φ is invariant under translation owing to the rephasing condition. Therefore, in the integration in Eq. (A5), $\chi(\boldsymbol{x}_1)$ can be replaced by $\chi_0(\boldsymbol{x}_1)$. Then, the integrand only yields nonzero contributions for the case if $|\boldsymbol{x}_1|$ is smaller than the size of the unit cell. Since, for sufficiently long T, $f_{\text{Gauß}}(\boldsymbol{x}_2-\boldsymbol{x}_1,T)$ describes a relatively broad particle distribution over many unit cells, $f_{\text{Gauß}}(\boldsymbol{x}_2-\boldsymbol{x}_1,T)\approx f_{\text{Gauß}}(\boldsymbol{x}_2,T)$, and one can approximate Eq. (A5) by

$$\begin{aligned}E_3(\boldsymbol{q}_1,\boldsymbol{q}_2,\boldsymbol{q}_3)\approx\tilde{\chi}_0(\boldsymbol{q}_1)\iint d\boldsymbol{x}_2 d\boldsymbol{x}_3\chi(\boldsymbol{x}_2)f_{\text{Gauß}}(\boldsymbol{x}_2,T/2)\\ \times e^{-i\boldsymbol{q}_2\cdot\boldsymbol{x}_2}\chi(\boldsymbol{x}_3)f_{\text{Gauß}}(\boldsymbol{x}_3-\boldsymbol{x}_2,T/2)\,e^{-i\boldsymbol{q}_3\cdot\boldsymbol{x}_3},\end{aligned} \tag{A6}$$

where $\tilde{\chi}_0(\boldsymbol{q})$ is the Fourier transform of $\chi_0(\boldsymbol{x})$. One can express Eq. (A6) as

$$\begin{aligned}E_3(\boldsymbol{q}_1,\boldsymbol{q}_2,\boldsymbol{q}_3)\approx\tilde{\chi}_0(\boldsymbol{q}_1)\iint d\boldsymbol{x}_2 d\boldsymbol{x}_3\chi(\boldsymbol{x}_2)H(\boldsymbol{x}_2,\boldsymbol{x}_3,T/2)\\ \times e^{-i\boldsymbol{q}_2\cdot\boldsymbol{x}_2}\chi(\boldsymbol{x}_3)e^{-i\boldsymbol{q}_3\cdot\boldsymbol{x}_3},\end{aligned} \tag{A7}$$

with

$$H(\boldsymbol{x}_2,\boldsymbol{x}_3,T)=f_{\text{Gauß}}(\boldsymbol{x}_2,T)f_{\text{Gauß}}(\boldsymbol{x}_3-\boldsymbol{x}_2,T). \tag{A8}$$

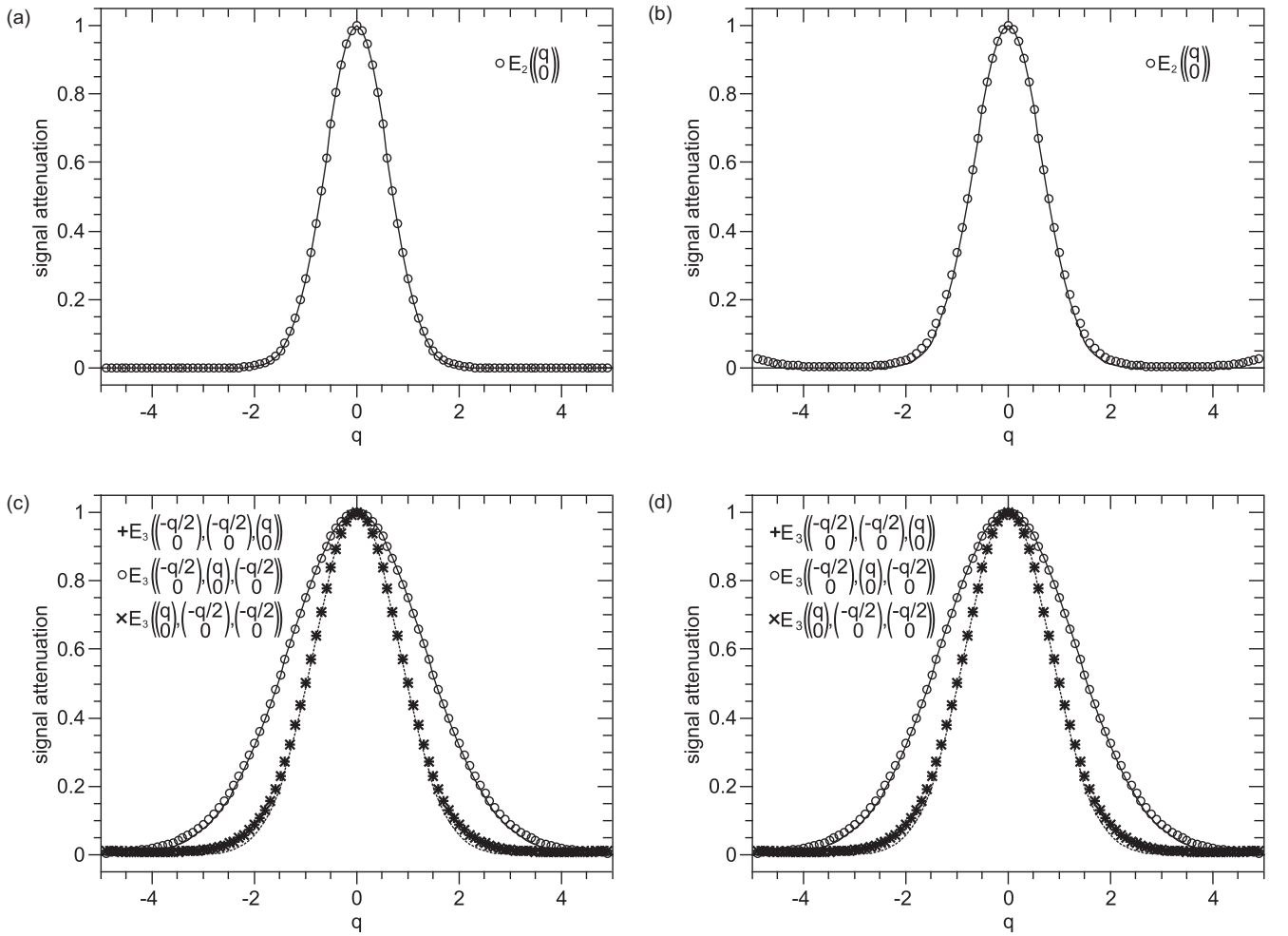

FIG. 8. Line broadening caused by finite diffusion time ($T = 3$) for the hexagonal lattice of cylinders [left column (a,c)] and for the cubic lattice of triangles [right column (b,d)]. The peak at $q = 0$ is displayed. Simulated values (dots) are well approximated by the Gaussian envelope model (line).

The Fourier transform of $H(\boldsymbol{x}_2,\boldsymbol{x}_3,T)$ is

$$\tilde{H}(\boldsymbol{q}_2,\boldsymbol{q}_3,T) = \exp[-(\boldsymbol{q}_2+\boldsymbol{q}_3)^{\mathrm{T}} \times \Sigma(\boldsymbol{q}_2+\boldsymbol{q}_3)/2 \; -\boldsymbol{q}_3^T\Sigma\boldsymbol{q}_3/2]. \quad \text{(A9)}$$

Using the convolution theorem, the signal attenuation can be written as

$$E_3(\boldsymbol{q}_1,\boldsymbol{q}_2,\boldsymbol{q}_3) \approx \tilde{\chi}_0(\boldsymbol{q}_1)\tilde{\chi}(\boldsymbol{q}_2)*|_{\boldsymbol{q}_2}\tilde{H}(\boldsymbol{q}_2,\boldsymbol{q}_3,T/2)*|_{\boldsymbol{q}_3}\tilde{\chi}(\boldsymbol{q}_3), \quad \text{(A10)}$$

where $*|_{\boldsymbol{q}_2}$ and $*|_{\boldsymbol{q}_3}$ denote convolutions with respect to $\boldsymbol{q}_2$ and $\boldsymbol{q}_3$, respectively. In the long-time limit, σ_{xx}^2 and σ_{yy}^2 become large and $\tilde{H}(\boldsymbol{q}_2,\boldsymbol{q}_3,T/2)$ becomes narrow. Thus, the signal attenuation is well approximated by

$$E_3(\boldsymbol{q}_1,\boldsymbol{q}_2,\boldsymbol{q}_3) \approx \tilde{\chi}_1(\boldsymbol{q}_1)\tilde{\chi}(\boldsymbol{q}_2)\tilde{\chi}(\boldsymbol{q}_3). \quad \text{(A11)}$$

As for $E_3(\boldsymbol{q}_1,\boldsymbol{q}_2,\boldsymbol{q}_3)$, one finds the signal attenuation for the two-gradient-pulse profile $G_{\boldsymbol{q},-\boldsymbol{q}}$, (t):

$$E_2(\boldsymbol{q}) \approx \tilde{\chi}_0(\boldsymbol{q})[\tilde{f}_{\mathrm{Gauß}}(\boldsymbol{q},T) * \tilde{\chi}(-\boldsymbol{q})], \quad \text{(A12)}$$

where $\tilde{f}_{\mathrm{Gauß}}(\boldsymbol{q},T) = \exp(-\boldsymbol{q}^T\Sigma\boldsymbol{q}/2)$ is the Fourier transform of $f_{\mathrm{Gauß}}(\boldsymbol{x},T)$. This equation differs slightly from the one given by Callghan (Eq. (7.33) in [1] on page 392). In our notation, Callaghan's formula reads $E_2(\boldsymbol{q}) \approx |\tilde{\chi}_0(\boldsymbol{q})|^2\tilde{f}_{\mathrm{Gauß}}(\boldsymbol{q}-\boldsymbol{q}_{\mathrm{peak}}T)$, where $\boldsymbol{q}_{\mathrm{peak}}$ denotes the peak position in q space. The difference originates from the different use of the Gaussian envelope model. Callaghan assumes that the hopping probability from pore to pore is Gaussian, while it is assumed here that the particle displacement is Gaussian.

Now, an approximate formula for the line broadening at $q = 0$ is provided. Using the definitions $\boldsymbol{q}_1 = q\boldsymbol{v}_1$, $\boldsymbol{q}_2 = q\boldsymbol{v}_2$, and $\boldsymbol{q}_3 = q\boldsymbol{v}_3$ and using that $\tilde{\chi}_0(\boldsymbol{q}) \approx 1$ for small $\boldsymbol{q}$, Eq. (A11) becomes

$$E_3(q\boldsymbol{v}_1,q\boldsymbol{v}_2,q\boldsymbol{v}_3) \approx \tilde{H}(q\boldsymbol{v}_2,q\boldsymbol{v}_3,T) = \exp\left\{-\frac{q^2}{2}[(\boldsymbol{v}_2+\boldsymbol{v}_3)^{\mathrm{T}} \times \Sigma(\boldsymbol{v}_2+\boldsymbol{v}_3)+\boldsymbol{v}_3^T\Sigma\boldsymbol{v}_3]\right\}. \quad \text{(A13)}$$

Figure 8 visualizes the line broadening of the signal peak at $q = 0$ for the two considered lattices. The line representing the Gaussian envelope model and the simulated data (dots) are in good agreement.

Interestingly, the line broadening of $E_3(\boldsymbol{q}_1,\boldsymbol{q}_2,\boldsymbol{q}_3)$ depends on the time ordering of the peaks: For instance, the peak is broader if the gradient pulse of double amplitude is applied in

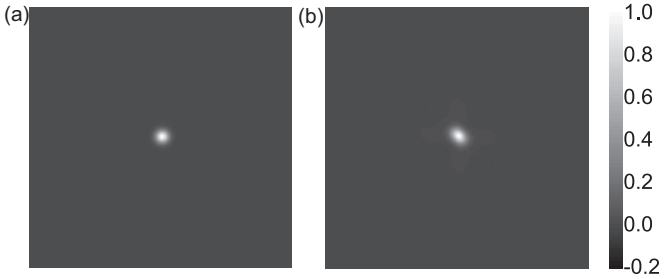

FIG. 9. Signal attenuation obtained with the long-narrow gradient profile for the hexagonal cylinder lattice (a) and the rectangular lattice of triangles (b) for $|q_x| \leqslant 10\pi$ and $|q_y| \leqslant 10\pi$. σ_{Lx} and σ_{Ly} are zero and the image matrix is of size 200×200.

between the two smaller gradient pulses compared to applying it before or after them.

APPENDIX B: LONG-NARROW GRADIENTS

The long-narrow gradient profile $\boldsymbol{G}_{\text{long-narrow}}(t) = \gamma^{-1}\boldsymbol{q}[T^{-1} - \delta(t - T)]$, which is well suited to obtain diffusion pore images of closed pores [38], cannot be used for diffusion lattice imaging. This is visualized in Fig. 9, where the long-narrow signal attenuation is plotted and where it is apparent that peaks do not arise. Consequently, the lattice cannot be reconstructed. This can be explained as follows. During the first gradient, the particle obtains the phase that corresponds to the phase of a particle that stays still at the center of mass of the particle trajectory. The second gradient yields a phase only depending on the trajectory end point. In diffusion pore imaging, the center of mass of the first trajectory converges towards the center of mass of the pore thus enabling a sharp image reconstruction. In a connected lattice, however, such a convergence does not take place; the trajectory center of mass can be located anywhere, even inside the solid matrix. Therefore, the distance between the center of mass and the end point of the trajectory, which determines the signal, is not directly related to the lattice structure. This broad distribution of trajectory centers of mass leads to a large peak broadening, which eventually obscures the peaks. Thus, for open, well-connected pores, the approach's success for closed pores cannot be simply transferred, but new techniques have to be employed.

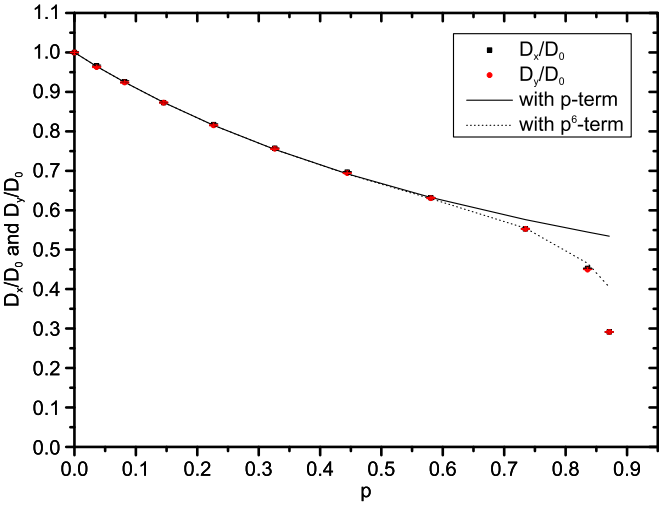

FIG. 10. Long-time diffusion coeffiecient. The theoretical estimate according to Eq. (C1) (lines) and Monte Carlo simulation results (dots) are shown. The error bars at the dots are too small to be well perceivable.

APPENDIX C: LONG-TIME DIFFUSION COEFFICIENT IN THE HEXAGONAL ARRAY OF CYLINDERS

To estimate the linewidths for the cylinder lattice, the classical findings of Lord Rayleigh for the rectangular array of cylinders [75] can be extended to the case of a hexagonal cylinder packing to find the effective diffusion coefficient D_∞ in the long-time limit, which is related to Σ by $\Sigma = 2D_\infty T$ in the long-time limit:

$$D_\infty/D_0 \approx \frac{1 - 2p\left(1 + p - \frac{135}{64}\frac{p^6}{\pi^6}S_6^2\right)^{-1}}{1 - p}, \qquad \text{(C1)}$$

where p is the packing density, i.e., the volume fraction of the solid matrix, D_0 is the free diffusion coefficient, and $S_n = \sum_{m\neq 0, m'\neq 0}(m' + im)^{-n}$, where the sum runs over all cylinder positions for m and m'. For example, some possible values for m and m' are (1,0), $(1,\sqrt{3})$, $(1/2,\sqrt{3}/2)$, and $(1/2, -\sqrt{3}/2)$. Numerically we find $S_6 \approx 5.8630$. Figure 10 shows the long-time diffusion coefficients obtained with Monte Carlo simulations and the prediction by Eq. (C1). Although Eq. (C1) is a series expansion for small p, it is remarkable that it is well valid for quite large packing densities.

[1] P. T. Callaghan, *Principles of Nuclear Magnetic Resonance Microscopy* (Clarendon Press, Oxford, UK, 1991).
[2] D. K. Jones, *Diffusion MRI: Theory, Methods, and Applications* (Oxford University Press, New York, 2011).
[3] M. E. Moseley, J. Kucharczyk, J. Mintorovitch, Y. Cohen, J. Kurhanewicz, N. Derugin, H. Asgari, and D. Norman, Am. J. Neuroradiol. **11**, 423 (1990).
[4] K.-O. Lövblad, P. M. Jakob, Q. Chen, A. E. Baird, G. Schlaug, S. Warach, and R. R. Edelman, Am. J. Neuroradiol. **19**, 201 (1998).
[5] M. C. Roethke T. A. Kuder, T. H. Kuru, M. Fenchel, B. A. Hadaschik, F. B. Laun, H.-P. Schlemmer, and B. Stieltjes, Invest. Radiol. **50**, 483 (2015).
[6] C. Lin, E. Itti, A. Luciani, C. Haioun, M. Meignan, and A. Rahmouni, Cancer Imaging **10** (1A), S172 (2010).
[7] C. Lin, A. Luciani, E. Itti, T. El-Gnaoui, A. Vignaud, P. Beaussart, S. J. Lin, K. Belhadj, P. Brugières, E. Evangelista, C. Haioun, M. Meignan, and A. Rahmouni, Eur. Radiol. **20**, 2027 (2010).
[8] J. H. Jensen, J. A. Helpern, A. Ramani, H. Lu, K. Kaczynski, Magn. Reson. Med. **53**, 1432 (2005).

[9] H. Lu, J. H. Jensen, A. Ramani, and J. A. Helpern, NMR Biomed. **19**, 236 (2006).

[10] A. M. Marschar, T. A. Kuder, B. Stieltjes, A. M. Nagel, P. Bachert, and F. B. Laun, J. Magn. Reson. Imaging **41**, 1581 (2014).

[11] J. Veraart, D. H. J. Poot, W. Van Hecke, I. Blockx, A. Van der Linden, M. Verhoye, and J. Sijbers, Magn. Reson. Med. **65**, 138 (2011).

[12] T. A. Kuder, B. Stieltjes, P. Bachert, W. Semmler, and F. B. Laun, Magn. Reson. Med. **67**, 1401 (2012).

[13] D. Le Bihan, E. Breton, D. Lallemand, M. L. Aubin, J. Vignaud, M. Laval-Jeantet, Radiology **168**, 497 (1988).

[14] A. Luciani, A. Vignaud, M. Cavet, J. T. Nhieu, A. Mallat, L. Ruel, A. Laurent, J. F. Deux, P. Brugieres, and A. Rahmouni, Radiology **249**, 891 (2008).

[15] A. Lemke, F. B. Laun, M. Klauss, T. J. Re, D. Simon, S. Delorme, L. R. Schad, and B. Stieltjes, Invest. Radiol. **44**, 769 (2009).

[16] A. Lemke, F. B. Laun, D. Simon, B. Stieltjes, and L. R. Schad, Magn. Reson. Med. **64**, 1580 (2010).

[17] A. Wetscherek, B. Stieltjes, and F. B. Laun, Magn. Reson. Med. **74**, 410 (2015).

[18] S. Mori and P. C. van Zijl, NMR Biomed. **15**, 468 (2002).

[19] R. Xue, P. C. van Zijl, B. J. Crain, M. Solaiyappan, and S. Mori., Magn. Reson. Med. **42**, 1123 (1999).

[20] P. J. Basser, S. Pajevic, C. Pierpaoli, J. Duda, and A. Aldroubi, Magn. Reson. Med. **44**, 625 (2000).

[21] B. Stieltjes, W. E.Kaufmann, P. C. van Zijl, K. Fredericksen, G. D. Pearlson, M. Solaiyappan, and S. Mori, NeuroImage **14**, 723 (2001).

[22] B. Stieltjes, R. M. Brunner, K. Fritzsche, and F. Laun, *Diffusion Tensor Imaging: Introduction and Atlas* (Springer, Heidelberg, Germany, 2012).

[23] P. F. Neher, F. B. Laun, B. Stieltjes, and K. H. Maier-Hein, Magn. Reson. Med. **72**, 1460 (2014).

[24] X. Chen, D. Weigel, O. Ganslandt, M. Buchfelder, and C. Nimsky, NeuroImage **45**, 286 (2009).

[25] J. Kärger, J. Caro, P. Cool, M. O. Coppens, D. Jones, F. Kapteijn, F. Rodríguez-Reinoso, M. Stöcker, D. Theodorou, E. F. Vansant, and J. Weitkamp, Chem. Eng. Technol. **32**, 1494 (2009).

[26] J. Kärger and R. Valiullin, Chem. Soc. Rev. **42**, 4172 (2013).

[27] L. F. Gladden and J. Mitchell, New J. Phys. **13**, 035001 (2011).

[28] C. Vogt, P. Galvosas, N. Klitzsch, and F. Stallmach, J. Appl. Geophys. **50**, 455 (2002).

[29] N. Nestle, P. Galvosas, and J. Kärger, Cem. Concr. Res. **37**, 398 (2007).

[30] F. Stallmach and P. Galvosas, Annu. Rep. NMR Spectrosc. **61**, 51 (2007).

[31] G. Zheng and W. S. Price, J. Magn. Reson. **195**, 40 (2008).

[32] M. Nordin, M. N. Jacobi, and M. Nyden, J. Magn. Reson. **201**, 205 (2009).

[33] P. Galvosas and P. T. Callaghan, C. R. Phys. **11**, 172 (2010).

[34] F. Marica, S. A. B. Jofré, K. U. Mayer, B.J. Balcom, and T. A. Al, J. Contam. Hydrol. **125**, 47 (2011).

[35] M. E. Komlosh, E. Özarslan, M. J. Lizak, F. Horkay, V. Schram, N. Shemesh, Y. Cohen, and P. J. Basser, J. Magn. Reson. **208**, 128 (2011).

[36] B. Siow, I. Drobnjak, A. Chatterjee, M. F. Lythgoe, and D. C. Alexander, J. Magn. Reson. **214**, 51 (2012).

[37] D. S. Grebenkov, Rev. Mod. Phys. **79**, 1077 (2007).

[38] F. B. Laun, T. A. Kuder, W. Semmler, and B. Stieltjes, Phys. Rev. Lett. **107**, 048102 (2011).

[39] F. B. Laun, T. A. Kuder, A. Wetscherek, B. Stieltjes, and W. Semmler, Phys. Rev. E **86**, 021906 (2012).

[40] N. Shemesh, C. F. Westin, and Y. Cohen, Phys. Rev. Lett. **108**, 058103 (2012).

[41] V. G. Kiselev and D. S. Novikov, Phys. Rev. Lett. **110**, 109801 (2013).

[42] T. A. Kuder and F. B. Laun, Magn. Reson. Med. **70**, 836 (2013).

[43] F. B. Laun and T. A. Kuder, Magn. Reson. Imaging **31**, 1236 (2013).

[44] S. Hertel, M. Hunter, and P. Galvosas, Phys. Rev. E **87**, 030802(R) (2013).

[45] T. A. Kuder, P. Bachert, J. Windschuh, and F. B. Laun, Phys. Rev. Lett. **111**, 028101 (2013).

[46] S. A. Hertel, M. Hunter, and P. Galvosas, Microporous Mesoporous Mater. **205**, 44 (2015).

[47] S. A. Hertel, X. Wang, P. Hosking, M. Cather Simpson, M. Hunter, and P. Galvosas, Phys. Rev. E **92**, 012808 (2015).

[48] T. A. Kuder and F. B. Laun, Phys Rev E **92**, 022706 (2015).

[49] S. Stapf, R. A. Damion, and K. J. Packer, J. Magn. Reson. **137**, 316 (1999).

[50] P. P. Mitra, Phys. Rev. B **51**, 15074 (1995).

[51] E. Özarslan and P. J. Basser, J. Magn. Reson. **188**, 285 (2007).

[52] D. G. Cory and A. N. Garroway, Magn. Reson. Med. **14**, 435 (1990).

[53] P. T. Callaghan, D. MacGowan, K. J. Packer, and F. O. Zelaya, J. Magn. Reson. **90**, 177 (1990).

[54] P. T. Callaghan, A. Coy, D. MacGowan, K. J. Packer, and F. O. Zelaya, Nature **351**, 467 (1991).

[55] P. T. Callaghan, *Translational Dynamics and Magnetic Resonance* (Oxford University Press, New York, 2011).

[56] P. P. Mitra, P. N. Sen, L. M. Schwartz, and P. Le Doussal, Phys. Rev. Lett. **68**, 3555 (1992).

[57] P. T. Callaghan, A. Coy, T. P. J. Halpin, D. MacGowan, K. J. Packer, and F. O. Zelaya, J. Chem. Phys. **97**, 651 (1992).

[58] M. Matsumoto and T. Nishimura, ACM Trans. Model. Comput. Simul. **8**, 3 (1998).

[59] See Supplemental Material at http://link.aps.org/supplemental/10.1103/PhysRevE.93.032401 for MATLAB code generating the figures of the manuscript.

[60] L. M. Schwartz, D. J. Bergman, K. J. Dunn, and P. P. Mitra, Magn. Reson. Imaging **14**, 737 (1996).

[61] N. Shemesh, C. F. Westin, and Y. Cohen, Phys. Rev. Lett. **110**, 109802 (2013).

[62] H. Hauptman, Curr. Opin. Struct. Biol. **7**, 672 (1997).

[63] I. Uson and G. M. Sheldrick, Curr. Opin. Struct. Biol. **9**, 643 (1999).

[64] G. Taylor, Acta Crystallogr., Sect. D **59**, 1881 (2003).

[65] E. Weckert and K. Hümmer, Acta Crystallogr., Sect. A **53**, 108 (1997).

[66] D. J. Bergman and K. J. Dunn, Phys. Rev. E **52**, 6516 (1995).

[67] D. J. Bergman and K. J. Dunn,Phys. Rev. E **51**, 3401 (1995).

[68] D. J. Bergman, K.-J. Dunn, L. M. Schwartz, and P. P. Mitra, Phys. Rev. E **51**,3393 (1995).

[69] A. L. Sukstanskii, D. A. Yablonskiy, and J. J. Ackerman, J. Magn. Reson. **170**, 56 (2004).

[70] C. H. Ziener, S. Glutsch, P. M. Jakob, and W. R. Bauer, Phys. Rev. E **80**, 046701 (2009).
[71] F. B. Laun, S. Huff, and B. Stieltjes, Magn. Reson. Imaging **27**, 541 (2009).
[72] A. Moussavi-Biugui, B. Stieltjes, K. Fritzsche, W. Semmler, and F. B. Laun, Magn. Reson. Med. **65**, 190 (2011).
[73] E. Fieremans, Y. De Deene, S. Delputte, M. S. Özedemir, Y. D'Asseler, J. Vlassenbroeck, K. Deblaere, E. Achten, and I. Lemahieu, J. Magn. Reson. **190**, 189 (2008).
[74] P. Pullens, A. Roebroeck, and R. Goebel, J. Magn. Reson. Imaging **32**, 482 (2010).
[75] L. Rayleigh, Philos. Mag., Ser. 5 **34**, 481 (1892).